Experimental and theoretical study of the microstructure evolution and thermal-physical properties of hypereutectic Al–Fe alloys

Liling Mo[1], Mingxian Lin[1], Meiyan Zhan[1], Yu-Jun Zhao[2,a), Jun Du[1,3,a)]

[1] School of Materials Science and Engineering, South China University of Technology, Guangzhou 510640, China
[2] Department of Physics, South China University of Technology, 381 Wushan Rd, Guangzhou 510640, Guangdong, China
[3] Department of Metallic Materials, School of Materials Science and Engineering, South China University of Technology, 381 Wushan Rd, Guangzhou 510640, Guangdong, China
a) Address all correspondence to these authors. e-mails: zhaoyj@scut.edu.cn; tandujun@sina.com

A systematic investigation was undertaken to analyze the microstructure and thermal-physical properties of hypereutectic Al-xFe alloys. With increasing Fe content, the $Al_{13}Fe_4$ phase undergoes a morphological shift from needle-like to lamellar-like. The coarse $Al_{13}Fe_4$ negatively affects the thermal conductivity (TC), resulting in a decrease from 200.1 to 84.5 W/(m/K) of TC as the Fe content rises from 2 to 12 wt%. Simultaneously, the thermal expansion coefficient (CTE) decreases. At 100°C, Al-12Fe has a CTE of 17.6×10^{-6}/K. Additionally, first-principles calculations were used to understand the intrinsic properties of the $Al_{13}Fe_4$. Using the quasi-harmonic approximation (QHA), the linear CTE of $Al_{13}Fe_4$ at 100°C was calculated to be 9.88×10^{-6}/K. By integrating experiments and theoretical calculations, the generalized effective medium theory (GEMT) and a modified Turner model were employed to quantitatively describe the correlation between the microstructural evolution of Al-xFe alloys and their TC/CTE.

Introduction

Nowadays, the utilization of aluminum (Al) alloys in electronic and heat dissipation domains, such as cables and heat sinks, has been garnering escalating attention [1–3]. Therefore, there is an urgent need to develop cast Al alloys characterized by high thermal conductivity (TC), low thermal expansion coefficient (CTE), and commendable mechanical properties [4–7]. Iron (Fe) is a common impurity element in Al alloys. However, trace Fe addition hardly affects the TC of Al alloy for its low solubility in Al [8, 9]. Furthermore, Fe can combine with Al and form the $Al_{13}Fe_4$ phase, which possesses a low CTE. As a result, Al–Fe alloys are considered to have broad prospects for application in the field of heat dissipation.

The microstructures of Al–Fe alloys vary depending on the Fe content, which allows for their categorization into three types: hypoeutectic (Fe content < 1.8 wt%), eutectic (Fe content = 1.8 wt%) and hypereutectic (Fe content > 1.8 wt%) alloys. In the past few decades, extensive research has been conducted to explore the microstructural evolution, mechanical properties,

and their relationship of Al–Fe alloys [10–12]. In addition to high-temperature mechanical properties, high TC and low CTE are crucial for engineering applications. Chen et al. studied the microstructure, TC, and electrical conductivity (EC) of Al-(0.5 ~ 1.5)wt% Fe alloys, discovering that the measured TC matched the predicted values based on the Wiedemann-Franz law [13]. Besides, the series model was employed to elucidate the correlation between the microstructure and TC in hypoeutectic Al–Fe alloys [13]. Qi et al. prepared Al-2.5 wt% Fe alloy using the powder laser melting method, the tensile strength and TC were about 320 MPa and 150 W/(m/K) [14]. Jiang et al. carried out modification treatment on Al-0.5 wt% Fe alloy by adding a small amount of lanthanum (La), La addition could simultaneously improve the mechanical and electrical properties of the Al-0.5 wt% Fe alloy [15]. Luo et al. found that adding a moderate amount of cobalt (Co) improved both the TC and mechanical properties of the Al-2 wt% Fe alloy [16]. The increase in TC was attributed to the refining effect on the primary Al_3Fe (also known as $Al_{13}Fe_4$) phase.

The thermal-physical properties, like EC/TC/CTE of Al–Fe alloys, are closely linked to microstructural evolution. As the concentration of low-solubility elements rises, the volume fraction of the second phase is heightened and there is a tendency for both TC and CTE to decrease. Theoretical modeling is a commonly used method to quantify the correlation between microstructural evolution and thermal properties [7, 13, 17]. TC models mainly include the solute atom, series, parallel, Maxwell, effective medium theory (EMT) models, etc. [13, 17–21]. While the commonly used theoretical models for predicting CTE include the rule of mixture (ROM), Turner, Kerner, and Schapery models [7, 22–25]. These models are closely related to the microstructure, phase composition, and intrinsic properties of phases. However, acquiring experimental data for phase properties is challenging, resulting in insufficient related data. Theoretical simulations based on the first-principles calculation have become effective methods for analyzing TC, mechanical and thermal expansion properties, and can reveal the thermodynamic properties and structural stability of intermetallic compounds [26–28].

Here, the influence of Fe content on the microstructure, EC, TC, and CTE of binary Al-xFe alloys was systematically studied first. Subsequently, the intrinsic properties of $Al_{13}Fe_4$ (e.g., mechanical and thermal properties) were analyzed by the theoretical calculations. By combining experiments, theoretical calculations, and mathematical models, the relationships between the microstructural revolution and TC/CTE were quantified. The obtained results offer enhanced insights into the correlation

between microstructure and TC/CTE within Al-xFe alloys, thereby presenting invaluable information to design alloys that possess excellent TC and thermal expansion properties.

Results

Microstructure and thermal-physical properties

Microstructures and phase composition of Al-xFe alloys

The optical and SEM results of Al-xFe alloys with varying Fe contents are shown in Figs. 1 and 2. The Al-2Fe alloy primarily exhibits a eutectic structure. Upon increasing the Fe content to 4 wt%, the primary Fe-rich phases precipitate in the form of block and needle-like. As the Fe content continues to rise, both the size and quantity of the primary phases increase. When the Fe content reaches 10 wt% and 12 wt%, the alloy consists of a substantial amount of block-like and needle-like Fe-rich phases, which form a distinct interface with the Al matrix. Figure 1(f) illustrates the XRD patterns of the Al-xFe alloys, confirming the existence of cubic α-Al and monoclinic $Al_{13}Fe_4$ (Al_3Fe) phases. The planes of α-Al are (111), (200), (220), (311) and (222). The (105), (006), (202), (111), (014), (113) and (313) planes are detected for $Al_{13}Fe_4$ phase. Figure 2 displays the SEM and EDS results of the Al-xFe alloys. Based on the size and morphology of the intermetallic compounds, it is possible to clearly distinguish between the primary and eutectic structures. The black matrix represents α-Al, the network, and feather-like structures
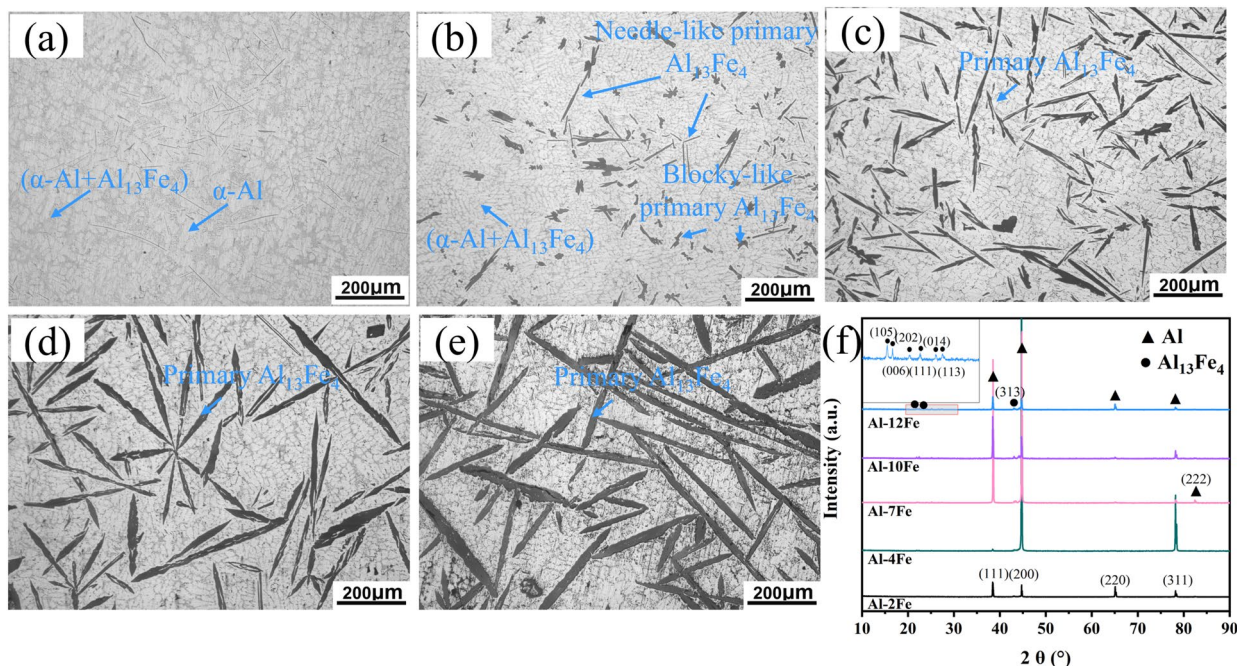

Figure 1: (a–e) Optical microstructures of Al-xFe alloys (x = 2 ~ 12 wt%): (a) Al-2Fe, (b) Al-4Fe, (c) Al-7Fe, (d) Al-10Fe, (e) Al-12Fe, (f) XRD patterns of Al-xFe alloys.
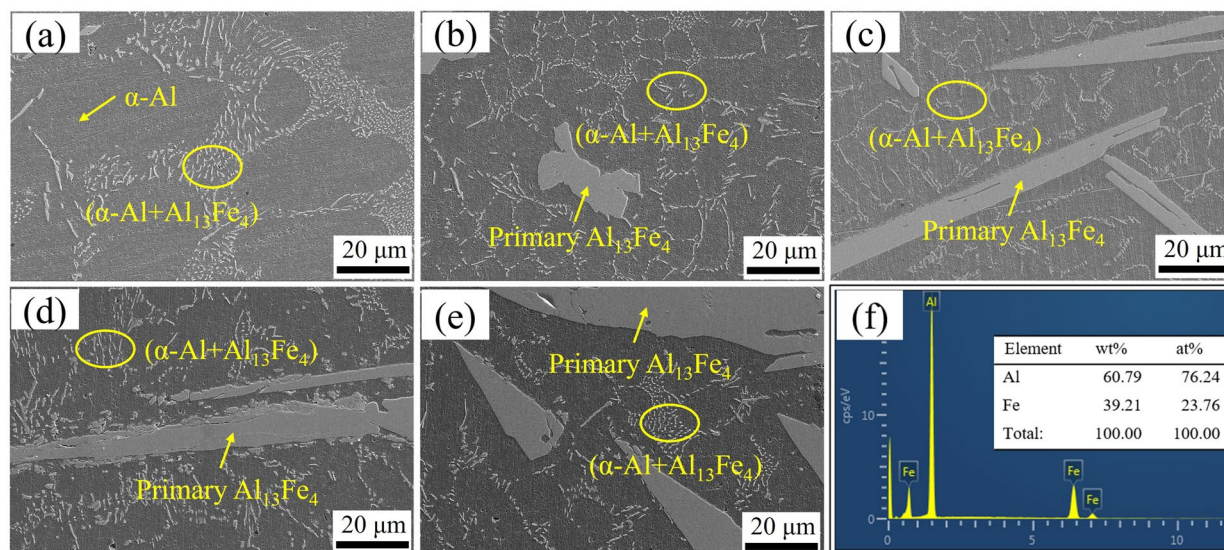
Figure 2: SEM images of Al-xFe alloys ($x = 2 \sim 12$ wt%): (a) Al-2Fe, (b) Al-4Fe, (c) Al-7Fe, (d) Al-10Fe, (e) Al-12Fe, (f) the EDS results of the primary $Al_{13}Fe_4$ phase.

represent (α-Al + $Al_{13}Fe_4$) eutectic structure, and the plate-like, rod-like, and sheet-like structures are the primary $Al_{13}Fe_4$ phases. As the Fe content increases, there is a distinct alteration in the morphology of the primary $Al_{13}Fe_4$, transitioning from short plate to elongated rod-like. The average size of the primary $Al_{13}Fe_4$ phase is counted and depicted in Fig. S1, which increases as the Fe content increases. For the eutectic $Al_{13}Fe_4$ phase, its morphology is unchanged with the change of Fe content.

Thermal-physical properties and hardness of Al-xFe alloys

The EC, thermal diffusivity (α), density (c), and heat capacity (Cp) of the Al-xFe alloys were determined through experiments. Subsequently, the TC was calculated using the obtained values of α, ρ, and Cp. These TC values of Al-xFe alloys are illustrated in Fig. 3. As presented in Fig. 3(a), a notable exponential decrease in α is observed with the increase of Fe content. Compared to Al (with Cp = 0.9 J/(g/K)), Fe possesses a lower Cp of 0.44 J/(g/K). Thus, the total Cp of the alloy exhibits a linear decrease as Fe content increases. Concurrently, the ρ of the Al–Fe alloy increases with rising Fe content. Overall, both EC/TC display

a linear decrease with increasing Fe content. In the case of the Al-2Fe alloy, the EC and TC are measured as 30.4 MS/m and 200.1 W/(m/K). As for Al-12Fe alloy, the EC and TC drop to 10.9 MS/m and 84.5 W/(m/K), respectively.

The CTEs changed with temperature and Fe content of Al-xFe alloys are shown in Fig. 4. The decrease in the CTE indicates an improvement in the thermal expansion property. As seen in Fig. 4, the CTEs of Al-xFe alloys decrease as the Fe content increases. In addition, for Al–Fe alloys with the same composition, the CTE curve initially increases sharply and then levels off as the temperature increases. As the Fe content increases, the volume fraction of $Al_{13}Fe_4$ increases, resulting in a decrease in the CTE from 20.6×10^{-6}/K for Al-2Fe to 17.6×10^{-6}/K for Al-12Fe at 100°C.

The Vickers hardness of Al-xFe alloys is shown in Fig. S2. With the increase of Fe content, the hardness increases from 125.9 HV for Al-2Fe alloy to 236.0 HV for Al-12Fe alloy. This is related to the properties of the $Al_{13}Fe_4$ phase. As the Fe content increases, there is a corresponding rise in the volume fraction of the primary $Al_{13}Fe_4$ phase, contributing to an increase in the hardness as a result.
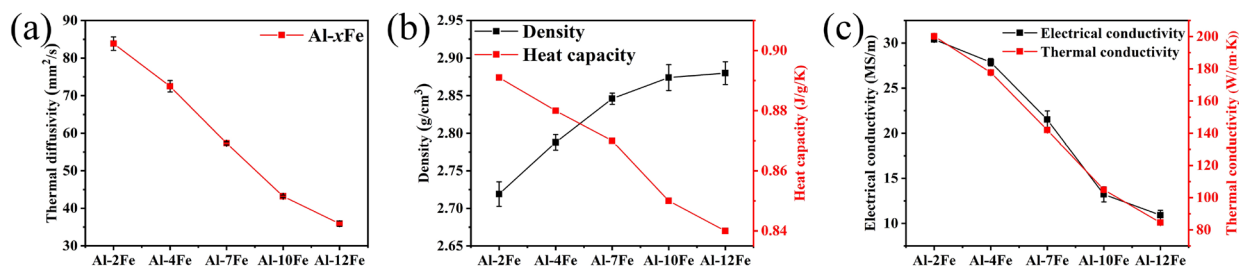

Figure 3: (a) Thermal diffusivity, (b) density and heat capacity, (c) electrical/thermal conductivity of Al-xFe alloys ($x = 2 \sim 12$ wt%).
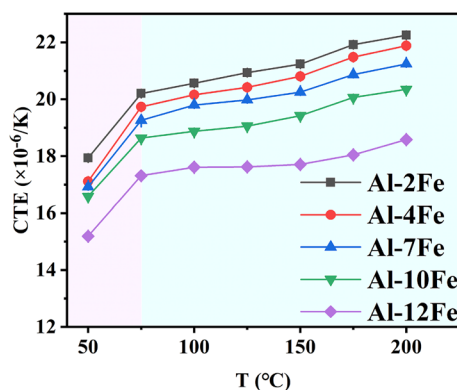
Figure 4: Thermal expansion coefficients (CTEs) changed with temperature and Fe content of Al-*x*Fe alloys (*x* = 2 ~ 12 wt%).

Theoretical calculation

Structural stability

The presence of α-Al and $Al_{13}Fe_4$ were experimentally identified. For identifying the most stable configuration in the Al–Fe system, formation enthalpies of different crystal structures were calculated through Al and Fe substitution at various composition ratios. In the actual fusion processes, the substituting components are usually in the same lattice structure to maintain high solubility. Here, FCC (Al), BCC (Fe) and FCC (Fe) were considered. The total entropy of 198 structures of the Al–Fe system with 2 to 5 times the cell volume was calculated using Eq. (1):

$$\Delta H = \frac{H_{Al_xFe_y} - xH_{Al} - yH_{Fe}}{(x+y)} \quad (1)$$

here, $H_{Al_xFe_y}$, H_{Al}, H_{Fe} denote the total energies of intermetallic compounds, and Al/Fe elements, *x* or *y* is the Al/Fe number in the intermetallic compounds.

A negative formation enthalpy indicates the thermodynamic stability of a structure. The formation enthalpies of Al–Fe alloys are depicted in Fig. 5(a), which considers configurations ranging from 2 to 5 times of the supercell, along with common Al–Fe compounds such as Al_6Fe, Al_9Fe_2, $Al_{13}Fe_4$, Al_3Fe, Al_8Fe_5, AlFe, $AlFe_2$, and $AlFe_3$. The black lines connect the most stable structure, determined by the lowest formation enthalpy. The majority of configurations exhibit negative formation enthalpies, indicating their stability. Additionally, the $Al_{13}Fe_4$ structure used in this work is the most stable at the corresponding concentration. Figure 5(b) illustrates the crystal structure of $Al_{13}Fe_4$. The $Al_{13}Fe_4$ belongs to the C2/m space group with lattice parameters of *a* = 15.43 Å, *b* = 8.04 Å, *c* = 12.44 Å, *α* = *γ* = 90°, and *β* = 107.73°. The formation enthalpy (Δ*H*) of $Al_{13}Fe_4$ is − 0.37 eV/atom, consistent with the literature [30].

Electronic properties

For a more profound understanding of the intrinsic properties of $Al_{13}Fe_4$, the electronic properties were studied through the analysis of the band structure and density of states (DOS). The investigation of the band structure and DOS reveals an overlap between the valence and conduction bands, further confirming the metallic properties of $Al_{13}Fe_4$ (as shown in Fig. S3). Additionally, by calculating the partial density of states (PDOS) of $Al_{13}Fe_4$, it becomes evident that the *d* electrons of the Fe element make a significant contribution to the physical properties. This indicates a crucial role for the *d* electrons of Fe in influencing the physical properties and behaviors of $Al_{13}Fe_4$.

Elastic properties

The calculation of elastic constants (C_{ij}) was undertaken to explore the mechanical properties of both Al and $Al_{13}Fe_4$ from theoretical insights. Different crystal systems possess distinct independent
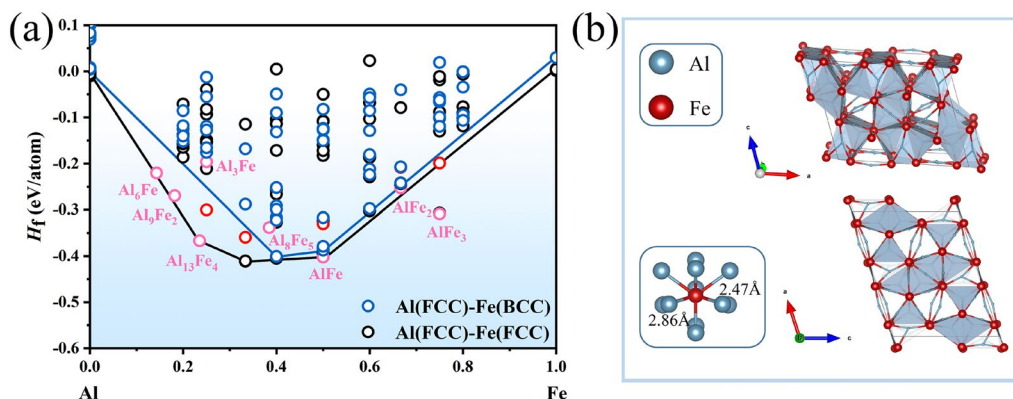

Figure 5: (a) The formation enthalpies of Al–Fe alloys with different configurations considered in 2 to 5 supercells. The black lines connect the most stable structures with the lowest formation enthalpy, while the pink circles represent common Al–Fe compounds calculated in this work. The results obtained from Aflow are denoted by red circles [29]. (b) The crystal structures of $Al_{13}Fe_4$.

elastic constants. Al belongs to the cubic system with 3 independent elastic constants of C_{11}, C_{12} and C_{44}. $Al_{13}Fe_4$ belongs to the monoclinic system, which encompasses C_{11}, C_{22}, C_{33}, C_{44}, C_{55}, C_{66}, C_{12}, C_{13}, C_{23}, C_{15}, C_{25}, C_{35}, and C_{46}. The values of these calculated results are presented in Table S1. According to the stability criterion for mechanical properties proposed by Born and Huang [31–33], it can be concluded that both Al and $Al_{13}Fe_4$ exhibit stable mechanical properties.

Using the independently calculated C_{ij}, the bulk modulus (B_H), shear modulus (G_H), Young's modulus (E), Poisson's ratio (v), and Debye temperature (θ_D) for both Al and $Al_{13}Fe_4$ were estimated. The calculated B_H and G_H are primarily associated with the Voigt upper and Reuss lower bounds [34, 35]. In the case of cubic and orthorhombic systems, the bulk modulus entails B_R and B_V, while the shear modulus incorporates G_R and G_V [36]. Ultimately, B_H, G_H, E, v, and θ_D can be calculated by the following formulas [33]:

$$B_H = \frac{B_V + B_R}{2} \tag{2}$$

$$G_H = \frac{G_V + G_R}{2} \tag{3}$$

$$E = \frac{9B_H G_H}{3B_H + G_H} \tag{4}$$

$$v = \frac{3B_H - 2G_H}{2(3B_H + G_H)} \tag{5}$$

$$\theta_D = \frac{h}{k_B} \left(\frac{3n}{4\pi} \left(\frac{N_A D}{M} \right) \right)^{1/3} \frac{1}{3} \left(\frac{2}{v_t^3} + \frac{1}{v_l^3} \right)^{-1/3} \tag{6}$$

$$v_t = \sqrt{\frac{G_H}{\rho}} \tag{7}$$

$$v_l = \sqrt{(B + 4G_H/3)/\rho} \tag{8}$$

here, B_R and B_V correspond to the bulk modulus for the Reuss lower and Voigt upper bounds. Similarly, G_R and G_V represent the shear modulus. N_A, h, and k_B denote Avogadro's, Plank's, and Boltzmann's constants, respectively. M, n and ρ refer to the atomic mass, atomic number and density of the unit cell,

respectively. V_t and V_l represent the velocities of the vertical and horizontal elastic waves in polycrystalline solids.

Table 1 presents the calculated B_V, B_R, B_H, G_V, G_R, G_H, B_H/G_H ratio, E, v, ρ, v_t, v_l, v_m and θ_D for Al and $Al_{13}Fe_4$. According to Table 1, the G_H and E of $Al_{13}Fe_4$ are 76.62 and 190.03 GPa, both higher than those of Al. Therefore, $Al_{13}Fe_4$ exhibits better resistance to deformation and greater stiffness. Additionally, the B_H/G_H ratio of $Al_{13}Fe_4$ is less than 1.75, indicating it is a brittle phase, whereas Al is a ductile phase. For solid materials, the critical value for v is 0.26, where values greater or smaller than 0.26 indicate ductility or brittleness. The v of $Al_{13}Fe_4$ is 0.24, showing a similar trend to the B_H/G_H ratio. The θ_D plays a crucial role in structural stability and bond strength. Materials with higher θ_D generally possess stronger chemical bonds and higher lattice thermal conductivity. The θ_D for Al and $Al_{13}Fe_4$ are 437.43 K and 601.67 K. In summary, $Al_{13}Fe_4$ exhibits enhanced bond strength and lattice thermal conductivity compared to Al.

Thermal-physical properties of Al and $Al_{13}Fe_4$

An analysis of the linear CTE, Bv, Cp and Grüneisen coefficient varies with temperature was conducted. To obtain the equilibrium volume corresponding to the lowest energy, the static total energies for 22 different volumes of both Al and $Al_{13}Fe_4$ were calculated. The data was then fitted using the Brich-Murnaghan equation [37, 38]. As illustrated in Fig. S4, the total energy of both Al and $Al_{13}Fe_4$ initially decreases and then increases with volume. Fig. S4(a) and (c) illustrate the change in Helmholtz free energy with volume for Al and $Al_{13}Fe_4$ across a temperature range from 0 to 1000 K. The red line connects the volumes, temperatures and free energies corresponding to the lattice equilibrium state. With increasing temperature, the Helmholtz free energy decreases, and an increase in the equilibrium volume at the state of lowest energy is observed. This is attributed to the growing contributions from vibrational entropy and lattice thermal expansion. Moreover, it can be observed that Al exhibits a greater tendency for expansion compared to $Al_{13}Fe_4$.

Temperature-dependent variations of the thermodynamic parameters for Al and $Al_{13}Fe_4$ are presented in Fig. 6. Both Al and $Al_{13}Fe_4$ exhibit an exponential increase in linear CTE at low temperatures. However, the curve for $Al_{13}Fe_4$ exhibits a gentler slope, indicating a smaller CTE compared to Al. This suggests

TABLE 1: The calculated bulk modulus (B_V, B_R, B_H), shear modulus (G_V, G_R, G_H), B_H/G_H, Young's modulus (E), density (ρ), longitudinal wave (v_t), shear wave (v_l), average acoustic velocity (v_m) and Debye temperature (θ_D) of $Al_{13}Fe_4$ and Al.

Phase	Bulk modulus (GPa)			Shear modulus (GPa)			
	B_V	B_R	B_H	G_V	G_R	G_H	B_H/G_H
$Al_{13}Fe_4$	122.07	121.62	121.84	77.43	75.82	76.62	1.59
Al	78.64	78.64	78.64	31.09	29.33	30.21	2.60
Phase	E (GPa)	v (GPa)	ρ (kg/m³)	v_l (m/s)	v_t (m/s)	v_m (m/s)	θ_D (K)
$Al_{13}Fe_4$	190.03	0.24	3.90×10^3	7.59×10^3	4.44×10^3	4.91×10^3	601.67
Al	80.35	0.33	2.71×10^3	6.62×10^3	3.34×10^3	3.74×10^3	437.43

that Al$_{13}$Fe$_4$ possesses a superior thermal expansion property. Figure 6(b) depicts the trend of decreasing Bv with rising temperature. This decline in Bv signifies a decrease in the ability of both Al and Al$_{13}$Fe$_4$ to resist external deformation, indicating that they become softer as the temperature rises. The Cp represents the absorbed energy that the material for each unit temperature increases. The solid heat capacity is mainly contributed by the lattice heat capacity except for the extremely low temperature. As illustrated in Fig. 6(c), the Cp demonstrates an initial sharp increase followed by a more gradual rise with temperature, which is consistent with the Debye model [39]. According to the relationship between the C$_V$ and the C$_P$: $C_P = C_V + 9\alpha^2 BVT$, α is the volume expansion coefficient of the isothermal system. The Al$_{13}$Fe$_4$ has a lower CTE than Al, so its Cp is less than Al with the increase of temperature. Another parameter related to the CTE is the Grüneisen coefficient, which shows the anharmonic effect depends on the volume change in the crystal. The formula for the relationship between the macroscopic Grüneisen coefficient and the volume thermal expansion coefficient is $\alpha_V(T) = \frac{C_V \gamma_T}{B_T T}$. Figure 6(d) presents the Grüneisen coefficients, at temperatures near 0 K, the Grüneisen coefficient for Al$_{13}$Fe$_4$ is negative, but it quickly transitions to a positive value. In contrast, the Grüneisen coefficients for Al remain positive throughout. The reason for the difference in Grüneisen coefficients between Al and Al$_{13}$Fe$_4$ may be related to the distribution of atoms in the structure, and

the numerical trend is reflected in the thermal expansion coefficient. This further confirms the distinct thermal expansion characteristics of Al and Al$_{13}$Fe$_4$ under room temperature and high-temperature conditions.

Discussion

Effect of microstructure evolution on the thermal conductivity

The heat conduction process in solid crystals is the energy transfer process. For the metal materials, the energy carriers include electrons, phonons and other heat transfer carriers, as shown in Fig. S5 [40]. In the heat conduction process of metal materials, free electrons play a leading role. The adding elements mainly exist as solid solution atoms and precipitated phases, which scatter free electrons, leading to a reduction in their average free path.

The Al matrix has a very low solubility for Fe, causing excess Fe to precipitate in the form of Al$_{13}$Fe$_4$. In the near-eutectic Al-2Fe alloy, the microstructure is characterized by the presence of both the α-Al matrix and the (α-Al + Al$_{13}$Fe$_4$) eutectic structure, where the size of the Al$_{13}$Fe$_4$ eutectic is small. Therefore, the degree of free electron scattering is relatively weak, resulting in minimal impact on electron and phonon transport processes. Consequently, the Al-2Fe alloy
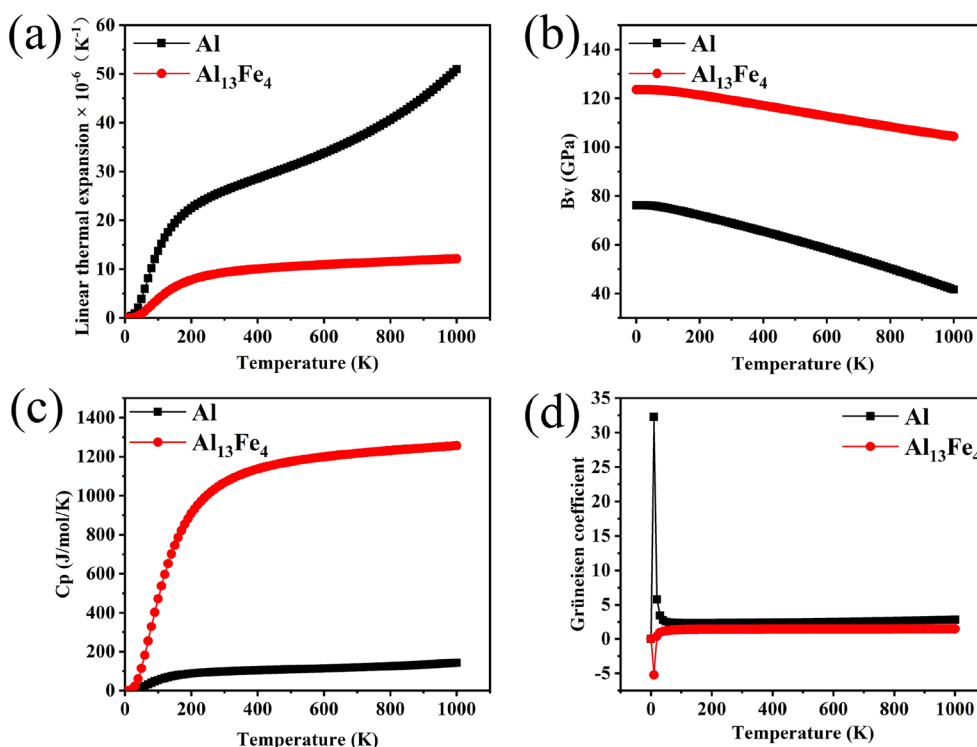

Figure 6: (a) The variation of linear expansion coefficient, (b) bulk modulus (Bv), (c) heat capacity (Cp) and (d) Grüneisen coefficient with temperature of Al$_{13}$Fe$_4$ and Al.

exhibits excellent TC with a value of 200.1 W/(m/K). However, with the increase in Fe content, the larger primary $Al_{13}Fe_4$ phase starts to precipitate, hindering the mobility of free electrons, then causing a linear decrease in both EC and TC. For Al-10Fe and Al-12Fe alloys, a significant amount of primary $Al_{13}Fe_4$ phases precipitate. The precipitated large plate-like primary $Al_{13}Fe_4$ phases have greater scattering effects on free electrons and completely block their transmission. Besides, the number of the α-Al with higher TC decreases to adversely affect the TC. The influence mechanism of free electron transport during the thermal conductivity by the precipitated $Al_{13}Fe_4$ is shown in Fig.S6 [41].

The relationship between TC and EC in metals is often described through the modified Wiedemann–Franz law: $\lambda = L \cdot T \cdot \sigma + C$ [42]. Here, λ, L, T and σ are the TC (W/(m/K)), Lorentz constant ($L = 2.45 \times 10^{-8}$ W/Ω/K^2), Kelvin temperature (K) and EC (MS/m), respectively. C is a constant. The ratio of EC to TC is an independent constant. For the Al-xFe alloys, L was determined to be 2.1×10^{-8} W/Ω/K^2 and C was selected as 11.7 W/(m/K) [6, 43]. The TC can be calculated utilizing the modified Wiedemann–Franz law, the calculated and experimental TC for the Al-xFe alloy is illustrated in Fig. 7. A notable linear correlation is observed in the hypereutectic Al-xFe alloys, with an R^2 value of 0.996, signifying the significant role of electrons in the heat transfer process of this binary alloy.

The analysis of the relationship between microstructural evolution and TC in Al-xFe alloys can be conducted by the application of the generalized effective medium theory (GEMT) model. The α-Al and $Al_{13}Fe_4$ coexist in a randomly interpenetrating manner in the Al–Fe alloy, with a higher volume fraction of the $Al_{13}Fe_4$ phase distributed within dendritic gaps. Within

the GEMT model, the Al-xFe alloy is considered a composite material consisting of two phases. Thus, the GEMT model enables the examination of the correlation between microstructure evolution and TC in Al-xFe alloys [41, 44, 45]:

$$\lambda = \frac{\sum_{i=1}^{m} \lambda_i V_i \frac{d_i k_0}{(d_i-1)k_0+\lambda_i}}{\sum_{i=1}^{m} V_i \frac{d_i k_0}{(d_i-1)k_0+\lambda_i}} \qquad (9)$$

λ_i, V_i are the TC, volume fraction of different phases, d_i denotes the heat conduction mode, m represents the component fraction, k_0 denotes the parameter related to the shape factor. Here, $d_i = 3$ refer to the reference [46].

The optimization of the shape factor is achieved by minimizing the Euler distance, which describes the difference between two matrices. A smaller Euler distance suggests that the calculated TC value is in closer agreement with the experimental TC. The optimization outcomes of the shape factor are illustrated in Fig. 8(a), revealing that the minimum Euler distance is achieved when $n = 6$. Furthermore, the volume fraction of the α-Al and $Al_{13}Fe_4$ was determined using Image Pro Plus software, as depicted in Fig. S7(c). The TC of the Al matrix is assumed to be $\lambda_m = 258$ W/(m/K), while the TC of $Al_{13}Fe_4 = 24$ W/(m/K) [6]. The fitting results of the GEMT model and the experimental data are depicted in Fig. 8(b), demonstrating the capability of the GEMT model to offer reasonably accurate predictions for hypereutectic Al-xFe alloys.

Correlation between the microstructure and thermal expansion properties

The volume fraction of the $Al_{13}Fe_4$ phase gradually rises from Al-2Fe to Al-12Fe alloys. This results in a decrease in the alloy's CTE. At lower temperatures, the overall crystalline structure of the Al–Fe alloy primarily undergoes elastic deformation in response to temperature changes, resulting in a linear increase in CTE with temperature. However, as the temperature continues to rise, the Al matrix undergoes plastic deformation and interacts with the $Al_{13}Fe_4$ phase. The presence of the $Al_{13}Fe_4$ phase effectively impedes the deformation of the Al matrix, resulting in a smoother CTE curve.

The thermal expansion characteristics of Al-xFe alloys can be predicted using theoretical models. Various models have been proposed to estimate the CTE in composites reinforced with particles [7]. The Turner model is particularly adept at elucidating the thermal expansion characteristics of hypereutectic Al alloys. The expression for the Turner model is as follows [47]:

$$\alpha_c = \frac{\alpha_p V_p B_p + \alpha_m V_m B_m}{V_p B_p + V_m B_m} \qquad (10)$$

V_p, V_m represent the volume fraction of the second phase and the matrix, B_p, B_m denote the corresponding bulk
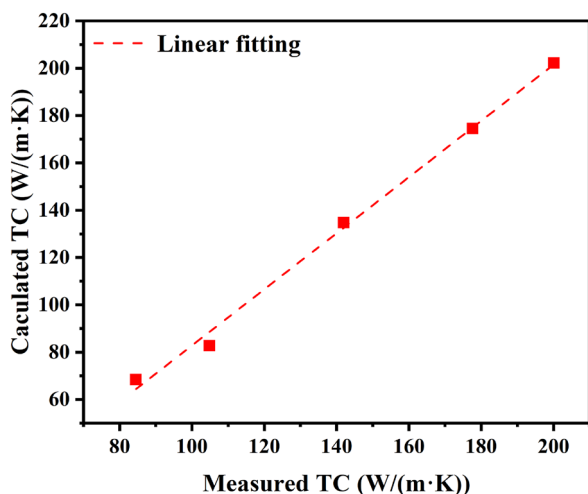

Figure 7: The measured and calculated thermal conductivity by the modified Wiedemann–Franz law of Al-xFe alloys ($x = 2 \sim 12$ wt%).
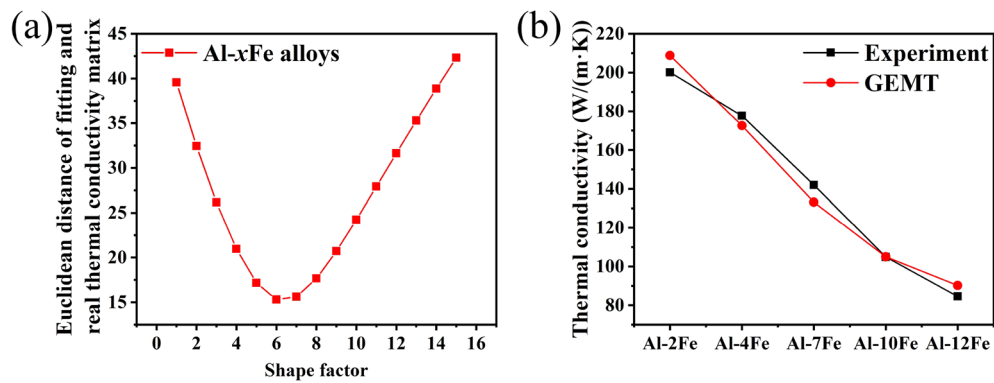
Figure 8: (a) The shape factor optimized by the Euler distance, (b) the GEMT model fitting results and experiments for the thermal conductivity of Al-xFe alloys ($x = 2 \sim 12$ wt%).

modulus. α_c, α_p, α_m represent the linear CTE of the composite, second phase and matrix, respectively.

Through the aforementioned first-principles calculation method, the linear CTE and bulk modulus were determined. Furthermore, their volume fractions were quantified using the Image Pro Plus software, as depicted in Fig. S7. Then CTEs of the alloys are predicted by the Turner model and illustrated in Fig. 9(a). However, discrepancies between the predicted values

and the experimental results are observed, particularly at the low temperature level.

To enhance the accuracy for predicting the CTE of hypereutectic Al–Fe alloys, the Turner model was optimized by introducing the composite modulus B_C. The composite volume modulus of the Al-xFe alloy was calculated using Eq. (11) [7] and depicted in Fig. 9(b). G_m represents the shear modulus of the matrix. It should be noted that $Al_{13}Fe_4$ undergoes
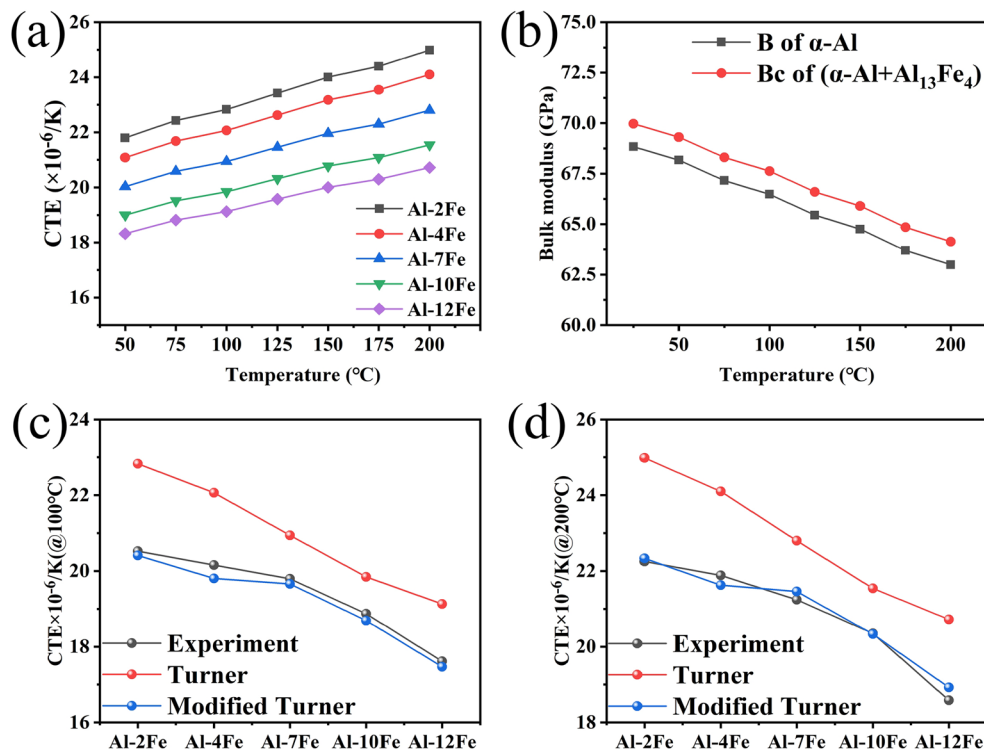

Figure 9: (a) The calculated thermal expansion coefficients of Al-xFe alloys by the Turner model. (b) The composite volume modulus. (c–d) The comparison of the experimental values and the prediction of Turner and modified Turner models of CTE for Al-xFe alloys at 100°C, 200°C ($x = 2 \sim 12$ wt%).

separation in the primary and eutectic structures, and the eutectic structure (α-Al + Al$_{13}$Fe$_4$) is considered a distinct phase.

$$B_c = \frac{\frac{V_p B_p}{3B_p + 4G_m} + \frac{V_m B_m}{3B_m + 4G_m}}{\frac{V_p}{3B_p + 4G_m} + \frac{V_m}{3B_m + 4G_m}} \quad (11)$$

Figure 9(c–d) present the comparison of the experimental values and the prediction of Turner and modified Turner models of CTE for Al-xFe alloys at 100°C, 200°C. For hypereutectic Al–Fe alloys, the modified Turner model displays a stronger correlation with experimental results compared to the original Turner model. Nonetheless, certain small discrepancies are observed, which may be attributed to experimental uncertainties and overlooked interfacial interactions.

Improvement of thermal properties of alloy

As the Fe content increases, the Al-xFe alloys exhibit enhanced thermal expansion properties attributed to the precipitation of the Al$_{13}$Fe$_4$ phase with a low CTE, while the TC is inevitably reduced for the coarse primary Al$_{13}$Fe$_4$ phase. Therefore, it is necessary to improve the TC by changing the structure of Al$_{13}$Fe$_4$ without negatively affecting CTE. According to the previous studies, an appropriate amount of Co can change the primary Al$_{13}$Fe$_4$ into particles in Al-2Fe alloy and improve the TC, mechanical properties at the same time [16]. Besides, Co modification can improve the TC without negatively affecting the CTE according to our ongoing work. The relationship between the TC and mechanical properties for commercial Al alloys, as well as the Ce/Co modified Al-2Fe alloys is shown in Fig. S8 [9, 16]. The developed Ce/Co modified Al-2Fe alloys have been proven to possess a combination of quantified TC and mechanical properties [9, 16]. Besides, the introduction of Sm/Yb to Al-7Fe alloy can alter the morphology of the lath-shaped primary Al$_{13}$Fe$_4$, transforming it into block and radial forms, and simultaneously improving the TC and thermal expansion properties [48]. Further research on the modification treatment, casting and deformation process should be performed to develop alloys with comprehensive TC, thermal expansion and mechanical properties, which can be used in electronic components.

Conclusions

This study comprehensively explored the microstructure, thermal-physical properties and their relationship of Al-xFe alloys with different Fe contents. Through experimental analysis, first-principles calculations and utilization of TC/CTE models, conclusions can be drawn as follows:

(1) Within hypereutectic Al-xFe alloys, the primary Al$_{13}$Fe$_4$ phase and (α-Al + Al$_{13}$Fe$_4$) eutectic structures coexist. As the Fe content increases, a notable transformation in the morphology of the primary Al$_{13}$Fe$_4$ is observed, shifting from fine block-like to coarse plate-like.

(2) Both the TC and CTE of Al-xFe alloys exhibit a decreasing trend as the Fe content rises. The TC shows a decline from 200.1 W/(m/K) in Al-2Fe to 84.5 W/(m/K) in Al-12Fe alloy. At 100°C, the CTE decreases from 20.6×10^{-6}/K to 17.6×10^{-6}/K as the Fe content increases from 2 to 12 wt%, showing an improved thermal expansion property.

(3) The structural stability, elasticity, and thermodynamic properties of Al$_{13}$Fe$_4$ were investigated by employing first-principles calculations, which reveal that Al$_{13}$Fe$_4$ demonstrates outstanding thermal expansion characteristics with a linear CTE of 9.88×10^{-6}/K (at 100°C).

(4) Through an integration of experiments and theoretical calculations, TC and CTE models were employed to establish a quantitative correlation between microstructural evolution and thermo-physical properties. By utilizing the GEMT and modified Turner models, accurate predictions of TC and CTE for Al-xFe alloys were achieved.

Experiments and theoretical calculations

Material and methods

By utilizing pure Al (Al ≥ 99.8, wt%, the same below) and an Al-20Fe master alloy, the Al-xFe alloys (where x = 2, 4, 7, 10, 12) were fabricated. The raw materials were carefully positioned in a crucible and subjected to heating in a resistance furnace, raising the temperature to over 50 °C above the liquidus temperature of the Al-xFe alloys. The liquidus temperature was predicted by the JMatPro software, as listed in Table S2. After the raw materials were completely melted, the melt was stirred with a ceramic rod for 2 ~ 5 min, then held for 10 ~ 30 min. Next, the refining agent and slag removal agent (commercial products of YT-J-1 and YT-D-4, respectively) were added to the melt, holding for 2 ~ 5 min and removing the slag at the top of the crucible. Finally, the molten alloy was poured into a preheated steel mold with a size of $100 \times 60 \times 15$ mm^3.

Samples for microstructure observation and thermal-physical, mechanical properties testing were sectioned from the ingot and then prepared using standard metallographic techniques, followed by an etching treatment with 0.5 wt% HF. The microstructure analysis was conducted utilizing optical microscope (Leica DMI 3000, Leica, Germany) and scanning electron microscope (SEM, Zeiss Gemini 300, Carl Zeiss, Germany). The phase constitution was determined by the X-ray diffraction (X 'PertPro MRD). To

quantify the chemical composition of phases, an energy dispersive spectrometer (EDS, Oxford X-MaxN, Oxford, UK) was employed. The thermal conductivity was assessed at room temperature, where a sample with a size of $\Phi 12.7\,\text{mm} \times 3\,\text{mm}$ was placed in a thermal conductivity meter (Netzsch LFA457) to obtain the thermal diffusivity (α). The Neumann–Kopp rule was used to calculate the constant pressure heat capacity (Cp) [49]. The density (ρ) was determined by Archimedes drainage method through a precision density balance (XHB-3000Z II). Then the TC λ was obtained using the formula: $\lambda = \alpha \cdot \rho \cdot Cp$ [50]. The CTE was measured using TMA Q400, with the sample subjected to heating from 25 to 200°C with a heating rate of 5°C/min in the nitrogen atmosphere. Vickers hardness was assessed with a load and holding time of 1000 and 10 s by an HVS-10 A digital display Vickers hardness tester. Ten points were tested on each sample, and the average value was taken.

Theoretical calculation details

The calculations were conducted using the Vienna ab-initio Simulation Package (VASP), with the interaction between ions and electrons described through the projector augmented wave (PAW) method [51]. The exchange–correlation energy of electrons was calculated using the Perdew-Burke-Ernzerhof (PBE) function within the generalized gradient approximation (GGA) [52]. A cutoff energy of 400 eV was chosen based on convergence tests. The Monkhorst–Pack scheme was applied for Brillouin zone sampling by employing a k-point grid of $10 \times 10 \times 10$. For structural optimization, the energy and force convergence criteria were set as 1×10^{-6} eV and less than 0.01 eV/Å. The thermal properties of intermetallic compounds were analyzed by the density functional perturbation theory (DFPT) and the quasi-harmonic approximation (QHA) method, based on the VASP and Phonopy packages [53–55]. For calculating the force constants, a supercell of dimensions $2 \times 2 \times 1$ was employed.

Acknowledgments

Author contributions

LM: Formal analysis, writing—original draft. ML: Formal analysis. MZ: Formal analysis. JD: Supervision, writing—review and editing. YZ: Supervision, writing—review and editing.

Funding

Data availability

The datasets supporting the conclusions of this article are included within the article and its additional files.

Declarations

Competing interests The authors declare that there are no known direct or potential conflict of interest which will affect the publish of this study.

Supplementary Information

The online version contains supplementary material available at https://doi.org/10.1557/s43578-024-01293-w.

References

1. W. Shih, C. Liu, W. Hsieh, Heat-transfer characteristics of aluminum-foam heat sinks with a solid aluminum core. Int. J. Heat Mass Transf. **97**, 742 (2016)

2. L.J.B. Smith, S.F. Corbin, R.L. Hexemer, I.W. Donaldson, D.P. Bishop, Development and processing of novel Aluminum powder metallurgy materials for heat sink applications. Metall. Mater. Trans. A **45**(2), 980 (2014)

3. J. Fang, Y. Zhong, M. Xia, F. Zhang, Mechanical and thermo-physical properties of rapidly solidified Al–50Si–Cu(Mg) alloys for thermal management application. Trans. Nonferrous Metals Soc. China. **31**(3), 586 (2021)

4. R.Y. Barkov, A.V. Mikhaylovskaya, O.A. Yakovtseva, I.S. Loginova, A.S. Prosviryakov, A. Pozdniakov, Effects of thermomechanical treatment on the microstructure, precipitation strengthening, internal friction, and thermal stability of Al–Er-Yb-Sc alloys with good electrical conductivity. J. Alloys Compd. **855**, 157367 (2021)

5. M. Wang, K. Hu, G. Liu, X. Liu, Synchronous improvement of electrical and mechanical performance of A356 alloy reinforced by boron coupling nano-AlNp. J. Alloy. Compd. **814**, 152217 (2020)

6. F. Stadler, H. Antrekowitsch, W. Fragner, H. Kaufmann, E.R. Pinatel, P.J. Uggowitzer, The effect of main alloying elements on the physical properties of Al–Si foundry alloys. Mater. Sci. Eng. A **560**, 481 (2013)

7. C.L. Hsieh, W.H. Tuan, Thermal expansion behavior of a model ceramic–metal composite. Mater. Sci. Eng. A **460–461**, 453 (2007)

8. B.D. Saller, T. Hu, K. Ma, L. Kurmanaeva, E.J. Lavernia, J.M. Schoenung, A comparative analysis of solubility, segregation, and phase formation in atomized and cryomilled Al–Fe alloy powders. J. Mater. Sci. **50**(13), 4683 (2015)

9. G. Luo, X. Zhou, C. Li, J. Du, Z. Huang, Design and preparation of Al-Fe-Ce ternary aluminum alloys with high thermal

conductivity. Trans. Nonferrous Metals Soc. China. **32**(6), 1781 (2022)

10. N. Zhang, Q. Hu, Z. Ding, W. Lu, F. Yang, J. Li, 3D morphological evolution and growth mechanism of proeutectic FeAl$_3$ phases formed at Al/Fe interface under different cooling rates. J. Mater. Sci. Technol. **116**, 83 (2022)

11. W. Wang, N. Takata, A. Suzuki, M. Kobashi, M. Kato, High-temperature strength sustained by nano-sized eutectic structure of Al–Fe alloy manufactured by laser powder bed fusion. Mater. Sci. Eng. A (2022). https://doi.org/10.1016/j.msea.2022.142782

12. S. Feng, E. Liotti, A. Lui, M.D. Wilson, P.S. Grant, Nucleation bursts of primary intermetallic crystals in a liquid Al alloy studied using in situ synchrotron X-ray radiography. Acta Mater. (2021). https://doi.org/10.1016/j.actamat.2021.117389

13. J.K. Chen, H.Y. Hung, C.F. Wang, N.K. Tang, Thermal and electrical conductivity in Al–Si/Cu/Fe/Mg binary and ternary Al alloys. J. Mater. Sci. **50**(16), 5630 (2015)

14. X. Qi, N. Takata, A. Suzuki, M. Kobashi, M. Kato, Managing both high strength and thermal conductivity of a laser powder bed fused Al–25Fe binary alloy: effect of annealing on microstructure. Mater. Sci. Eng. A **805**, 140591 (2021)

15. H. Jiang, S. Li, Q. Zheng, L. Zhang, J. He, Y. Song, C. Deng, J. Zhao, Effect of minor lanthanum on the microstructures, tensile and electrical properties of Al-Fe alloys. Mater. Design. **195**, 10 (2020)

16. G. Luo, Y. Huang, C. Li, Z. Huang, J. Du, Microstructures and mechanical properties of Al-2Fe-xCo ternary alloys with high thermal conductivity. Materials. **13**(17), 3728 (2020)

17. H. Pan, F. Pan, R. Yang, J. Peng, C. Zhao, J. She, Z. Gao, A. Tang, Thermal and electrical conductivity of binary magnesium alloys. J. Mater. Sci. **49**(8), 3107 (2014)

18. C. Su, D. Li, A.A. Luo, T. Ying, X. Zeng, Effect of solute atoms and second phases on the thermal conductivity of Mg-RE alloys: a quantitative study. J. Alloy. Compd. **747**, 431 (2018)

19. S. Aksöz, Y. Ocak, N. Maraşlı, E. Çadirli, H. Kaya, U. Böyük, Dependency of the thermal and electrical conductivity on the temperature and composition of Cu in the Al based Al–Cu alloys. Exp. Thermal Fluid Sci. **34**(8), 1507 (2010)

20. Y. Huang, X. Zhou, J. Du, Microstructure, thermal conductivity and mechanical properties of the Mg–Zn–Sb ternary alloys. Met. Mater. Int. **27**(11), 4477 (2020)

21. R.L. Hamilton, O.K. Crosser, Thermal conductivity of heterogeneous two-component systems. Ind. Eng. Chem. Fund. **1**, 182 (1962)

22. D.K. Hale, The physical properties of composite materials. J. Mater. Sci. **11**, 2105 (1976)

23. E.H. Kerner, The elastic and thermo-elastic properties of composite media. Proc. Phys. Soc. B **69**, 808 (1956)

24. R.A. Schapery, Thermal expansion coefficients of composite materials based on energy principles. J. Compos. Mater. **2**(3), 380 (1968)

25. P.S. Turner, Thermal-expansion stresses in reinforced plastics. NIST J. Res. **37**, 239 (1946)

26. S. Rameshkumar, G. Jaiganesh, V. Jayalakshmi, Structural, phonon, elastic, thermodynamic and electronic properties of Mg–X (X = La, Nd, Sm) intermetallics: the first principles study. J. Magnes. Alloys. **7**(1), 166 (2019)

27. Z. Tong, H. Bao, Decompose the electron and phonon thermal transport of intermetallic compounds NiAl and Ni$_3$Al by first-principles calculations. Int. J. Heat Mass Transf. **117**, 972 (2018)

28. D. Wu, S. Ma, T. Jing, Y. Wang, L. Wang, J. Kang, Q. Wang, W. Wang, T. Li, R. Su, Revealing the mechanism of grain refinement and anti Si-poisoning induced by (Nb, Ti)B$_2$ with a sandwich-like structure. Acta Mater. **219**, 1–10 (2021)

29. S. Curtarolo, W. Setyawan, G.L.W. Hart, M. Jahnatek, R.V. Chepulskii, R.H. Taylor, S. Wang, J. Xue, K. Yang, O. Levy, M.J. Mehl, H.T. Stokes, D.O. Demchenko, D. Morgan, AFLOW: An automatic framework for high-throughput materials discovery. Comput. Mater. Sci. **58**, 218 (2012)

30. J.J. Plata, D. Usanmaz, P. Nath, Predicting the lattice thermal conductivity of solids by solving the Boltzmann transport equation: AFLOW-AAPL an automated, accurate and efficient framework. Mater. Sci. **1**, 11 (2016)

31. F. Mouhat, F.X. Coudert, Necessary and sufficient elastic stability conditions in various crystal systems. Phys. Rev. B **90**(22), 224104 (2014)

32. M. Born, K. Huang, *Dynamical Theory of Crystal Lattices* (Oxford University Press, Oxford, 1954)

33. R. Hill, The elastic behaviour of a crystalline aggregate. Proc. Phys. Soc. A **65**, 349 (1952)

34. A. Reuss, Berechnung der Fließgrenze von Mischkristallen auf Grund der Plastizitätsbedingung für Einkristalle. ZAMM-J. Appl. Math. Mech. **9**(1), 49 (1929)

35. C.M. Kube, M.D. Jong, Elastic constants of polycrystals with generally anisotropic crystals. J. Appl. Phys. **120**(16), 165105 (2016)

36. D. Connétable, O. Thomas, First-principles study of the structural, electronic, vibrational, and elastic properties of orthorhombic NiSi. Phys. Rev. B **79**(9), 094101 (2009)

37. F. Birch, Finite elastic strain of cubic crystals. Phys. Rev. **71**(11), 809 (1947)

38. F.D. Murnaghan, The compressibility of media under extreme pressures. Proc. Natl. Acad. Sci. U.S.A. **30**(9), 244 (1944)

39. X.L. Liu, B.K. VanLeeuwen, S.L. Shang, Y. Du, Z.K. Liu, On the scaling factor in Debye-Grüneisen model: a case study of the Mg–Zn binary system. Comput. Mater. Sci. **98**, 34 (2015)

40. H. Bao, J. Chen, X. Gu, B. Cao, A review of simulation methods in micro/nanoscale heat conduction. ES Energy Environ. (2018). https://doi.org/10.30919/esee8c149

41. M. Jiang, L. Mo, X. Zhou, X. Liu, M. Zhan, J. Du, Microstructure evolution and thermophysical properties of hypereutectic Al-Fe-Ni alloys. Int. J. Metalcast. (2023). https://doi.org/10.2139/ssrn.4184518

42. R.W. Powell, Correlation of metallic thermal and electrical conductivities for both solid and liquid phases. Int. J. Heat Mass Transf. **8**, 1033 (1965)

43. J.E. Hatch, *Aluminum: Properties and Physical Metallurgy* (ASM International, Almere, 1984)

44. R.P.A. Rocha, M.A.E. Cruz, Computation of the effective conductivity of unidirectional fibrous composites with AN interfacial thermal resistance. Numer. Heat Transf. Appl. **39**, 179 (2001)

45. G. Carotenuto, A. Buonanno, The effective thermal conductivity of packed beds of spheres for a finite contact area. Numer. Heat Transf. A Appl. **37**(4), 343 (2000)

46. J. Wang, J.K. Carson, M.F. North, D.J. Cleland, A new approach to modelling the effective thermal conductivity of heterogeneous materials. Int. J. Heat Mass Transf. **49**(17–18), 3075 (2006)

47. Z. Wei, P. Ma, H. Wang, C. Zou, S. Scudino, K. Song, K.G. Prashanth, W. Jiang, J. Eckert, The thermal expansion behaviour of SiCp/Al–20Si composites solidified under high pressures. Mater. Design. **65**, 387 (2015)

48. L. Mo, M. Jiang, X. Zhou, Y.J. Zhao, J. Du, Modification mechanisms of hypereutectic Al-Fe alloys treated by Sm/Yb addition: experiments and first-principles calculations. J. Alloys Compd. (2023). https://doi.org/10.1016/j.jallcom.2023.169786

49. J. Leitner, P. Voňka, D. Sedmidubský, P. Svoboda, Application of Neumann-Kopp rule for the estimation of heat capacity of mixed oxides. Thermochim. Acta **497**(1), 7 (2010)

50. A. Rudajevová, M. Staněk, P. Lukáč, Determination of thermal diffusivity and thermal conductivity of Mg–Al alloys. Mater. Sci. Eng. A **341**(1), 152 (2003)

51. G.G. Kresse, J.J. Furthmüller, Efficient iterative schemes for ab initio total-energy calculations using a plane-wave basis set. Phys. Rev. B **54**, 11169 (1996)

52. J.P. Perdew, K. Burke, M. Ernzerhof, Generalized gradient approximation made simple. Phys. Rev. Lett. **77**(18), 3865 (1996)

53. X. Gonze, Adiabatic density-functional perturbation theory. Phys. Rev. A **52**(2), 1096 (1995)

54. M.A. Blanco, E. Francisco, V. Luaña, GIBBS: isothermal-isobaric thermodynamics of solids from energy curves using a quasi-harmonic Debye model. Comput. Phys. Commun. **158**(1), 57 (2004)

55. A. Togo, I. Tanaka, First principles phonon calculations in materials science. Scripta Mater. **108**, 1 (2015)